JGR Space Physics

RESEARCH ARTICLE
10.1029/2020JA028187

Special Section:
Probing the Magnetosphere Through Magnetoseismology and Ultra-Low-Frequency Waves

Evolution of High-*m* Poloidal Alfvén Waves in a Dipole Magnetic Field

Thomas Elsden[1] **and Andrew Wright**[2]

[1]School of Physics and Astronomy, University of Leicester, Leicester, UK, [2]School of Mathematics and Statistics, University of St Andrews, St Andrews, UK

Key Points:
- Initially high-*m* poloidal ULF waves will rotate, tending toward a toroidal polarization
- Alfvén wave phase mixing drives radially outward motion along contours of Alfvén frequency
- We provide theoretical predictions to be considered in satellite observations of high-*m* ULF waves

Correspondence to:
T. Elsden,
te79@le.ac.uk

Citation:
Elsden, T., & Wright, A. (2020). Evolution of high-*m* poloidal Alfvén waves in a dipole magnetic field. *Journal of Geophysical Research: Space Physics*, *125*, e2020JA028187. https://doi.org/10.1029/2020JA028187

Received 1 MAY 2020
Accepted 16 JUL 2020
Accepted article online 10 AUG 2020

Abstract We investigate how initially high-*m*, poloidal Alfvén waves evolve using a numerical model solving the ideal, cold, linear magnetohydrodynamic (MHD) equations in a 2-D dipole coordinate system. The curved magnetic geometry provides a key difference between the poloidal and toroidal Alfvén frequencies of any one field line. A polarization rotation from poloidal toward toroidal predicted from the Cartesian box model theory still occurs but now with the waves following contours of Alfvén frequency, which moves the Alfvén wave *across* field lines. The structure of these contours depends on the harmonic mode along the field line and the equilibrium. We find that the amplitude peak of the poloidal mode moves significantly radially outward in time. When the typically observed azimuthal phase motion of such waves is included, hodograms show a polarization rotation from purely poloidal to a mixed poloidal/toroidal polarization at all locations. Such features could be used to help interpret satellite observations of Pc4-5 poloidal ultralow frequency (ULF) waves in Earth's magnetosphere.

Plain Language Summary Earth's curved magnetic field lines can oscillate (like waves on a string), at a range of frequencies with the lowest being termed ultralow frequency (ULF) waves. In this paper we consider a specific subset of these waves known as high-*m* poloidal Alfvén waves, which have the characteristic that the wavelength in the radial direction is much larger than that in the azimuthal (angular) direction. Such waves are of geophysical importance as they can interact with energetic particles that are trapped and drifting in Earth's magnetic field. This has implications for space weather effects with spacecraft operations being negatively affected by such interactions. We perform computer simulations of how these waves evolve in a curved magnetic field like that of the Earth. We show that the structure of these waves changes in time, in a way that is unique to the geometry of the magnetic field, with the development of complex spatial structure. We further comment on how these features could be looked for in satellite observations.

1. Introduction

Ultralow frequency (ULF) waves (~1 mHz to 1 Hz, Jacobs et al., 1964) are among the lowest-frequency oscillations of Earth's magnetosphere. They represent large-scale perturbations to Earth's magnetic and electric fields and have been shown to have a critical impact on many areas of magnetospheric research, for example, radiation belt dynamics (Elkington et al., 2003), aurora and associated field-aligned currents (e.g., Milan et al., 2001), and ring current energization (Murphy et al., 2014).

This paper deals with a particular class of ULF waves, namely, Alfvén waves with a large azimuthal wavenumber (high-*m*), which have received a great deal of attention over the last 40–50 years. These waves have a much shorter azimuthal (toroidal) wavelength than that in the radial (poloidal) direction, which makes them dominantly poloidally polarized. Both the theoretical and observational history of these waves are rich and as such will be dealt with in the following separate sections for clarity.

1.1. Theory

High-*m* poloidal Alfvén waves are most commonly thought to be generated by the drift or drift-bounce resonance mechanisms (Southwood et al., 1969). Energetic particles drifting around the Earth can interact with such low-frequency waves, when the time taken for a particle to drift across an azimuthal wavelength is comparable to the wave period or related to an integer number of bounce periods between the northern and southern ionospheres (Southwood & Kivelson, 1981, 1982). Once a poloidally polarized Alfvén wave has

been generated, how does it evolve? One of the first mentions of this evolution in the literature is by Radoski (1974), who derives an asymptotic solution for the poloidal and toroidal fields in a cylindrical magnetic geometry. The author concludes that the poloidal modes will decay in time and that energy tends to be deposited into the toroidal modes.

Mann and Wright (1995) studied the evolution of poloidal Alfvén waves in a Cartesian box model geometry, solving the equations of cold, ideal, linear magnetohydrodynamics (MHD) numerically. Critically in their model, there exists a gradient of the Aflvén speed in the radial direction, making the plasma inhomogeneous. This gradient causes phase mixing to occur (Heyvaerts & Priest, 1983; Mann et al., 1995), whereby neighboring field lines in a meridional plane drift out of phase due to their different natural frequencies. This time-dependent phase mixing reduces the radial (poloidal) wavelength over time, which scales as the phase-mixing length

$$L_{ph} = \frac{2\pi}{\omega_A' t}, \tag{1}$$

where $\omega_A' = d\omega_A/dx$, representing the Alfvén frequency gradient in the direction of inhomogeneity (see Mann et al., 1995, Equation 21). This reduction in radial scale length will continue through the time when the scales in the poloidal and toroidal directions are comparable, until the mode becomes fully polarized in the toroidal direction. This can be viewed as a polarization rotation from poloidal to toroidal, which bears out the previous theory of Radoski (1974). It should be noted here that the frequency remains constant throughout this rotation, since in a Cartesian box model with straight field lines, the poloidal and toroidal Alfvén eigenfrequencies of any one field line are the same. The numerical results from Mann and Wright (1995) were consolidated by analytical solutions using a multiple timescales analysis in a follow-up study (Mann et al., 1997).

However, in a more realistic curved magnetic geometry such as a dipole, the poloidal and toroidal Alfvén eigenfrequencies are substantially different (Radoski, 1967). Therefore a simple rotation while maintaining the same frequency should not be permissible. To this end, Leonovich and Mazur (1993) and subsequent papers by coauthors (e.g., Klimushkin, 2007; Klimushkin et al., 1995; Mager & Klimushkin, 2006) have delved into this problem in a curved magnetic geometry analytically, in great mathematical detail. The key insight gleaned from these works is that an initially poloidal Alfvén wave will still undergo such a polarization rotation, however to do so and remain at the same frequency, it will have to travel along contours of Alfvén frequency (see Klimushkin et al., 1995, Figure 2); Leonovich & Mazur, 1993, Figure 2.

To explain this concept, it is useful to consider the theoretical framework of Alfvén resonances in a 3-D magnetic geometry, as described by Elsden and Wright (2017) and Wright and Elsden (2016). These papers were aimed at treating the field line resonance (FLR) process (Southwood, 1974), typically for low-m Alfvén waves, but many of the concepts carry over to the present study. The authors discuss how, for any one driving frequency, there is a Resonant Zone set up between the poloidal and toroidal resonant surfaces. That is to say, at the poloidal surface, a poloidally polarized Alfvén wave will have the same frequency as a toroidally polarized Alfvén wave at the toroidal surface. In between these boundaries (the Resonant Zone), Alfvén waves of intermediate polarization (between poloidal and toroidal) can have this same frequency. The structure of the Resonant Zone and the contours of Alfvén frequency are dependent upon the magnetic field geometry, the equilibrium, and the field-aligned harmonic number of the mode (see Wright & Elsden, 2016, Figure 6, for further information). Such ideas will be further elucidated throughout this paper.

The question at the heart of this study is as follows: How does an initially poloidal Alfvén wave evolve in a magnetic field where the poloidal and toroidal Alfvén frequencies differ? We aim to study this phenomena with a numerical model specifically designed to resolve the extremely fine-scale structure generated during phase mixing. Results from these simulations will highlight aspects of the Cartesian theory that carry over into the 3-D regime and will test whether the results of the analytic theory of Leonovich and Mazur (1993) are borne out numerically. Furthermore, we will put such theoretical results into the context of recent observations and provide predictions in terms of what observers of these phenomena may expect to see.

1.2. Observations

Observations of poloidal Alfvén waves are ubiquitous in Earth's magnetosphere, and only a brief outline of the most relevant works is given here. The key areas to highlight in order to best guide the simulations are as follows: What generates high-m poloidal Alfvén waves? Where and when are they most observed? What

is their radial and azimuthal extent? What are typical azimuthal wavenumbers? What is the field-aligned structure? How do they evolve in time?

High-m poloidal Alfvén waves are most often observed in satellite data, due to the screening effects of the ionosphere preventing them from registering in ground magnetometer data (Hughes & Southwood, 1976). Observations of Hughes et al. (1978) are among the first to attribute radially polarized Pc5 waves (period 100 s) to generation by wave-particle interactions, namely, the drift-bounce resonance process. Singer et al. (1982) also attributed Pc4-5 poloidal Alfvén waves to this generation mechanism, further finding the waves to be radially localized, occurring over widths of 0.2–1.6 in L shell.

Takahashi et al. (1990) observed ion flux oscillations (energy ~100 keV) at the same frequency as a radially polarized Pc5 magnetic pulsation, directly observing the link between the waves and the particles. The wave in question had an azimuthal wavenumber $|m|$~110, was westward propagating, and had a second harmonic field-aligned structure (as expected for observing drift-bounce resonance Southwood & Kivelson, 1981). Statistical studies show in general that radially polarized Pc4-5 monochromatic waves can occur over all local times, though most often in the afternoon sector (Anderson et al., 1990; Kokubun et al., 1989) and around noon (Dai et al., 2015). They are often longitudinally extended, for example, over 1.5 to 8 hr MLT (Engebretson et al., 1992) and 10 hr in MLT (Shi et al., 2018). On the dayside they predominantly occur in the region $L < 7$, moving to $L > 7$ on the nightside, and tend to be localized over 2–3 R_E in radial extent (Anderson et al., 1990).

High-m poloidal Alfvén waves are also observed under a variety of different magnetospheric conditions. They have been observed in the recovery phases of geomagnetic storms (Le et al., 2017; Shi et al., 2018), after geomagnetic storms during low geomagnetic activity (Engebretson et al., 1992; Min et al., 2017; Takahashi, Oimatsu, et al., 2018) and in generally quiet times (Kokubun et al., 1989). They can further be driven by substorm-injected particles (James et al., 2013, 2016).

The azimuthal wavenumber is a key parameter in this study, as discussed in the theory section above, since it controls the poloidal scale length that is critical to the wave evolution. There have been observations of a large range of "high-m" numbers, for example, from $m \sim 38$ (Yeoman et al., 2012) to $m \sim 258$ (Shi et al., 2018), and consequently, simulations with a variety of wavenumbers will be performed in this study.

There have been many recent studies on very long lasting poloidal ULF waves, on the order of a few days. Table 1 of Shi et al. (2018) provides a good overview of these recent works. Such studies are of interest to the present work given that the polarization rotation from poloidal to toroidal can require many wave periods to be realized. Therefore modes that are quickly damped would not display such a rotation. One such observation by Sarris et al. (2009) displayed a polarization rotation from poloidal to a mixed toroidal/poloidal polarization, and the authors were able to explain this evolution using the Cartesian box model theory of Mann and Wright (1995).

A further consideration is the field-aligned structure, which will also be important from a modeling perspective as the results will show. Typically poloidal ULF wave observations attributed to the drift-bounce mechanism are second harmonic in nature (e.g., Anderson et al., 1990; Takahashi et al., 1990). However, recently, fundamental poloidal mode waves have been observed (Dai et al., 2013; Takahashi, Claudepierre, et al., 2018; Takahashi et al., 2013), with drift resonance being the most likely generation mechanism.

The final observational studies to mention are those that attribute the signals to effects specifically from the evolution of high-m poloidal Alfvén waves in a curved magnetic geometry, since after all that is what this paper looks to investigate numerically. Yeoman et al. (2012) observed using radar data (Yeoman et al., 2006) the presence of equatorially moving curved phase fronts. The structure and evolution of these curved fronts was explained (after an analytical treatment) essentially by the poloidal and toroidal Alfvén eigenfrequencies being different, that is, because of the curved magnetic geometry. Leonovich et al. (2015) (using the observations of Dai et al., 2013) go a step further by claiming to observe the spatial structure expected by the polarization rotation in a 3-D magnetic field.

The aim of this paper is to present a comprehensive numerical treatment of the evolution of initially high-m poloidal Alfvén waves in a dipole background magnetic field. In its essence this is a theoretical piece of work; however, it is hoped that the results displayed here could help to inform future observations of this phenomena. The paper is laid out as follows: section 2 describes the numerical model used for the simulations performed in this study. Section 3 presents the results together with significant discussion, from three

simulations, first for a single azimuthal wavelength, then for multiple wavelengths, and finally including azimuthal phase motion. Conclusions are drawn in section 4.

2. Numerical Model

The model used has been described at length in many previous studies (e.g., Elsden & Wright, 2017, 2018, 2019; Wright & Elsden, 2016; Wright et al., 2018) and will therefore only briefly be summarized here.

We adopt a field-aligned orthogonal coordinate system (α, β, and γ), based on a 2-D dipole background magnetic field, which is adapted for numerical efficiency (see section 2 of Wright & Elsden, 2016, for a full description of the scale factors describing the coordinates). The field-aligned system takes advantage of the underlying field geometry and therefore requires only a few grid points to be taken along a field line, allowing far greater resolution in the perpendicular directions to resolve the small scales that develop through Alfvén wave phase mixing. The first coordinate α labels L shells, β is the "azimuthal" coordinate in which the background magnetic field is invariant (2-D dipole), and γ is the field-aligned coordinate. We cast the linearized MHD equations for a cold plasma in these coordinates and solve numerically using the second-order leapfrog trapezoidal finite difference scheme (Zalesak, 1979). The equations solved are listed in dimensionless form as Equations 9–13 of Elsden and Wright (2017). To maintain numerical stability, the global time step used to advance the solution is chosen to satisfy the Courant-Friedrichs-Lewy (CFL) condition. Typically energy is conserved to one part in 10^4 at the end of a simulation.

The boundary conditions are the same in all of the simulations presented in this paper and are as follows. The radial inner (α_{min}) and outer (α_{max}) boundaries are held to be perfectly reflecting, imposed with a node of radial velocity ($U_\alpha = 0$). The boundaries in azimuth (β_{min} and β_{max}) are also perfectly reflecting with a node of azimuthal velocity ($U_\beta = 0$). These boundaries are intended to be far enough away from the wave processes of interest in the center of the simulation domain to be of little effect. In order to damp any perturbations that do reach the azimuthal boundaries, we employ dissipative buffer zones there. At the ionospheric end of the field lines, the perpendicular velocity has a node setting a perfectly reflecting condition there also. Only the Northern Hemisphere is solved over, with a symmetry condition imposed at the equator that halves the simulation domain for numerical efficiency. There is no resistivity or dissipation included in the main simulation domain outside of the dissipative buffer regions, making this ideal MHD. This choice was made to allow small scales to develop that affect the development of high-m poloidal Alfvén waves, as will be discussed in detail in the following sections.

A note on the choice of the 2-D dipole as opposed to similar but more sophisticated 3-D dipole numerical magnetospheric models which now exist (Wright & Elsden, 2020). The aim of this paper is to elucidate a fundamental plasma physics process numerically for the first time. In the 2-D dipole, there is a larger discrepancy between the poloidal and toroidal Alfvén eigenfrequencies than in a 3-D dipole. Using the 2-D dipole improves numerical efficiency given that the solution domain can be taken to be a smaller portion of the field line, while retaining a realistic difference in the poloidal to toroidal frequencies. Furthermore, it is not intended at this stage to embed the process of the time evolution of an initially high-m poloidal Alfvén wave in a realistically driven magnetospheric simulation but purely to study this process in a medium where the Alfvén eigenfrequencies change with polarization. Hence, the simpler 2-D dipole is better suited to this job.

3. Results

3.1. Single Azimuthal Wavelength

3.1.1. Initial Condition

We begin with the simplest setup to investigate the evolution of a high-m poloidal Alfvén wave in a curved magnetic field geometry. The simulation presented here is used to develop some of the key physics before moving on to more realistic scenarios. In dimensionless units, the simulation domain has a radial extent of α: $0.3 \rightarrow 0.6$, which if scaled by an appropriate length scale, $L_0 = 10\,R_E$ say, would coincide with L shells from three to six. Azimuthally, the waveguide extends over $-0.2 \leq \beta \leq 0.2$ ($-2\,R_E \leq \beta \leq 2\,R_E$), but only the innermost section of this is focused on where the relevant wave behavior develops. The simulation variables used here (U_α, B_α, etc.) are the real velocity ($\mathbf{u}$) and magnetic field ($\mathbf{b}$) perturbations scaled by various geometric factors and the background field strength B. Such variables are more convenient to work with from a simulation standpoint, and full details on these are given by Wright and Elsden (2016).

The important parameter of the initial condition is the ratio of the radial to azimuthal scale length. Figures 1a and 1b display the radial and azimuthal simulation velocities respectively (U_α and U_β), in the equatorial plane at the initial time, for a radial to azimuthal scale length ratio of 5. The results are presented in dimensionless units to retain the generality and further applicability of the results. Since α and β correspond to real space in the equatorial plane, the plots can be easily translated to real distances in the magnetosphere; for example, a distance of 0.1 in α implies a real distance of 1 R_E (assuming a normalizing length scale of $L_0 = 10\,R_E$). The scale length in β corresponds to an m number of ~150 for this case. The initial perturbations are set by the equations:

$$U_\alpha(\alpha,\beta,\gamma) = e^{-\frac{(\alpha-\alpha_0)^2}{\alpha_w^2}} f(\beta)\cos\left(\frac{\pi}{2}\frac{\gamma}{\gamma_{max}}\right), \tag{2}$$

$$U_\beta(\alpha,\beta,\gamma) = 2\frac{(\alpha-\alpha_0)}{\alpha_w^2} e^{-\frac{(\alpha-\alpha_0)^2}{\alpha_w^2}} g(\beta)\cos\left(\frac{\pi}{2}\frac{\gamma}{\gamma_{max}}\right), \tag{3}$$

where

$$f(\beta) = 1 - \tanh^2(k_\beta\beta) - \frac{1}{2}\left\{1 - \tanh^2(k_\beta(\beta-\beta_1))\right\} - \frac{1}{2}\left\{1 - \tanh^2(k_\beta(\beta+\beta_1))\right\}, \tag{4}$$

$$g(\beta) = \frac{1}{k_\beta}\left\{\tanh(k_\beta\beta) - \frac{1}{2}\left\{\tanh(k_\beta(\beta-\beta_1)) + \tanh(k_\beta(\beta+\beta_1))\right\}\right\}. \tag{5}$$

The parameters α_0 and α_w are set to 0.45 and 0.05, respectively, and define the center and width of the α dependence of the profiles. We consider the approximate scale length of the wave packet in α to be $2\alpha_w$, where α_w defines the half width at which the profile has decayed to a value of $1/e$. The value of γ_{max} is the largest value of γ indicating the value at the end of the field line, which here is $\gamma_{max} = 0.315$, chosen to give a realistic difference in the fundamental poloidal and toroidal frequencies. The cosine dependence results in the fundamental mode along the field line. Such an initial condition was chosen to minimize the presence of the compressional fast mode to purely focus on the Alfvén waves and results in satisfying the condition

$$\frac{\partial U_\alpha}{\partial\alpha} + \frac{\partial U_\beta}{\partial\beta} = 0, \tag{6}$$

such that $\partial B_\gamma/\partial t = 0$ (see Elsden & Wright, 2017, Equation 13) and the magnetic field is not compressed, leading to the decoupled poloidal mode (Singer et al., 1981). Given that the radial to azimuthal scale length ratio is large here, the initial condition is dominantly poloidally polarized as can be seen by the amplitudes of the color bars in Figures 1a and 1b, where $U_\alpha >> U_\beta$. The Alfvén speed is simply set to unity everywhere, since the changing field line length with radial distance provides a sufficient continuum in the Alfvén frequency profile for this study. For this reason, a normalizing time is not specified as comparison to specific frequencies based on using a uniform Alfvén speed would not be illuminating. Rather, times should be considered in relation to the local Alfvén period, which will be provided in the relevant sections. However, to show that the simulation values are in a reasonable range, consider a normalizing length of $L_0 = 10\,R_E$ and velocity $V_0 = 500$ km^{-1}, giving a time of $T_0 = 127.42$ s (frequency $f_0 = 7.85$ mHz), which will be referred to in the next section.

3.1.2. Temporal Evolution of High-*m* Alfvén Waves

Figures 1c–1f display contour plots of the absolute value $|U_\perp| = \sqrt{U_\alpha^2 + U_\beta^2}$ in the equatorial plane at four times in the simulation. This quantity is used to better track the overall evolution throughout the simulation when the Alfvén waves have a mixed polarization (between poloidal and toroidal). To give the dimensionless times context, the poloidal Alfvén wave period at $(\alpha,\beta) = (0.45, 0.0)$ is $\tau_{A_{pol}} = 1.342$ (frequency of 5.8 mHz using the example normalization of the previous section). In Figure 1c early in the simulation (time $t = 8.616 = 6.420\ \tau_{A_{pol}}$), the initial perturbation has phase mixed in the radial direction, reducing the radial wavelength as oscillations on different field lines drift out of phase in time. Faint curves can be seen emanating from the initial perturbation region. Figure 1d at the time of $t = 17.233$ shows how phase mixing has reduced the wavelength in α further, and fascinatingly, the peak amplitude is moving out from the central region along well defined curves. This evolution is further demonstrated in Figures 1e and 1f, where the wave packet continues to move away from the region where the initial condition was defined around

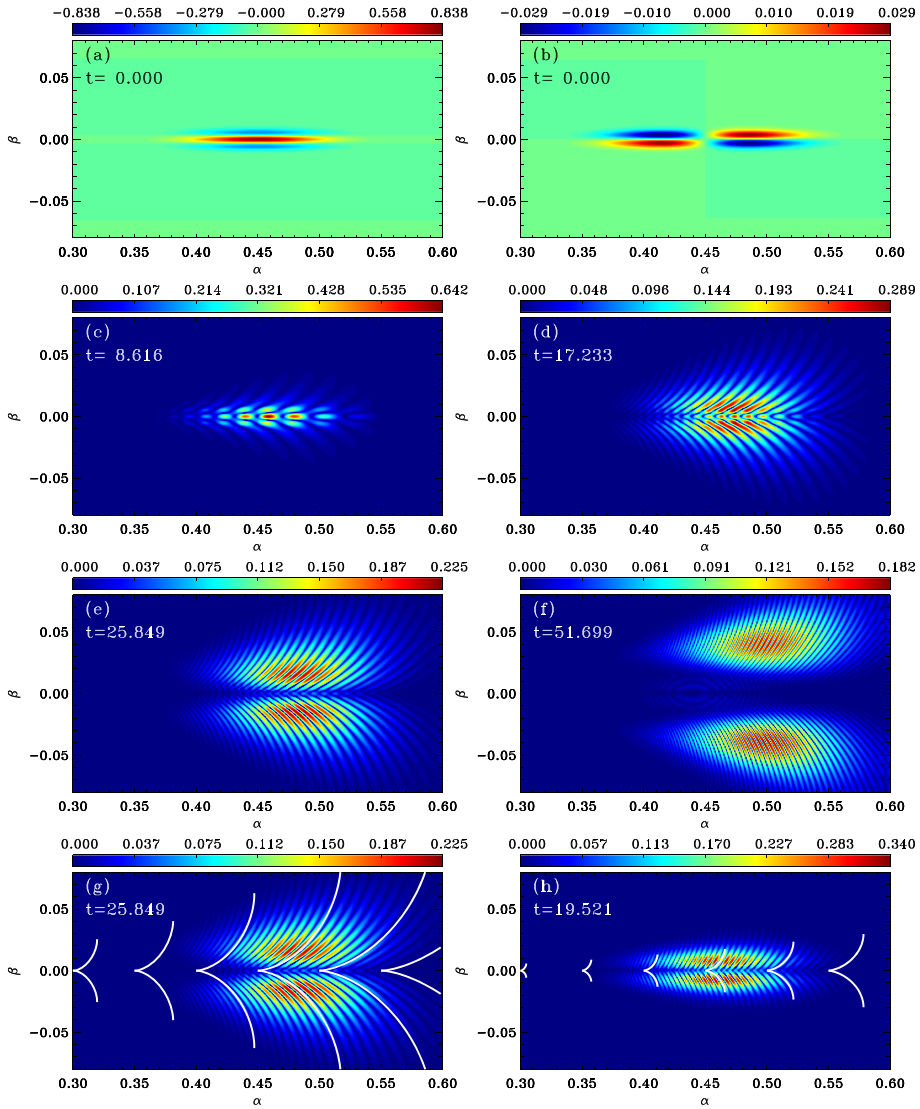

Figure 1. (a) Radial velocity U_α initial condition; (b) azimuthal velocity U_β initial condition; (c–f) color contours of $|U_\perp|$ in the equatorial plane at four different times as listed on the panels; (g) same as panel (e) with contours of Alfvén frequency overlaid in white for the fundamental mode along the field line; and (h) color contour of $|B_\perp|$ in the equatorial plane from a separate simulation for the second field-aligned harmonic. White contours are again of constant Alfvén frequency further described in the main text.

$\beta = 0$. This clearly demonstrates that the process of phase mixing of an initially poloidal Alfvén wave is very different in a dipole magnetic geometry than in the Cartesian box model regime (Mann & Wright, 1995).

In order to investigate the pattern traced out by the velocity contours in Figure 1, we considered that the curves could represent contours of Alfvén frequency. To explore this idea, we followed concepts presented by Wright and Elsden (2016) on solving the Alfvén wave equation adapted from Equation 9 of Singer et al. (1981), for an arbitrary polarization of the Alfvén wave. To define this polarization, we introduce new local coordinates (α' and β'), which represent a rotation of the previous axes (α and β) about the field-aligned axis by an angle θ, measured from the β axis. This angle represents the Alfvén wave polarization where the Alfvén wave is polarized along the β' axis, such that $\theta = 0$ implies the toroidal mode and $\theta = \pi/2$ the poloidal. For clarity, we reproduce Equation 23 of Wright and Elsden (2016) here:

$$\frac{\partial}{\partial\gamma}\left(\frac{1}{h_\gamma}\frac{\partial U_{\beta'}}{\partial\gamma}\right) + \frac{1}{h_\gamma}\frac{\partial}{\partial\gamma}\left(\ln\left(\frac{h_{\beta'}}{h_{\alpha'}}\right)\right)\frac{\partial U_{\beta'}}{\partial\gamma} + \frac{\omega_A^2}{V_A^2}h_\gamma U_{\beta'} = 0. \tag{7}$$

The derivatives are performed in the field-aligned direction γ; $\omega_A(\alpha', \beta', \theta)$ is the Alfvén frequency for the given location (α', β') and polarization θ and represents the eigenfrequency of Equation 7. Throughout the rest of this paper $\omega_A(\alpha', \beta', \theta)$ is referred to as the *Alfvén frequency*; V_A is the Alfvén speed; $h_{\alpha'}$, $h_{\beta'}$, and h_γ are scale factors describing the magnetic geometry, where the prime superscript denotes a rotation about the field-aligned axis as previously described; and $U_{\beta'}$ is a simulation variable related to the velocity perturbation aligned with this rotated direction.

From Equation 7 the Alfvén frequency ω_A can be found at any location for any polarization between poloidal and toroidal. We further surmised that since the mode begins with a poloidal polarization, it is the poloidal Alfvén frequency in the initial condition region that seeds the tracing of the curves apparent in Figure 1. Instead of calculating a frequency for a particular polarization, this can be reversed to find the polarization required for a given frequency. Therefore we can solve the Alfvén wave equation, asking what polarization of Alfvén wave is required to match this "seed" frequency. Mathematically speaking, we can trace curves satisfying

$$\omega_A(\alpha', \beta', \theta) = \omega_A(\alpha' = \alpha_1, \beta' = 0, \theta = \pi/2), \tag{8}$$

where (as previously stated) θ is the angle of Alfvén wave polarization between poloidal ($\theta = \pi/2$) and toroidal ($\theta = 0$) measured from the β axis, and α_1 is some location in α from where to start the contour tracing. Since the medium in the case presented in this paper is invariant in azimuth (β), the Alfvén frequency ω_A will also be independent of β. However we leave the more general expression listed in Equation 8 for future applications where the medium does vary with azimuth. In practice the curve sketching works by choosing a location $(\alpha', \beta') = (\alpha_1, 0)$ and then stepping in the α' direction to find the new polarization required to match the poloidal Alfvén frequency at the initial point. This polarization can then be used to step to a new point and the process repeated. In doing so, curves of constant Alfvén frequency can be traced and are the white lines overplotted in Figure 1g. Each pair of curves represents a different starting location in α' and hence a different poloidal Alfvén frequency. To be clear, at all points along each white line the Alfvén frequency is the same, it is merely the polarization that is changing. For example, the Alfvén frequency at $(\alpha', \beta') = (0.45, 0.0)$ for a poloidally polarized Alfvén wave is the same as at $(\alpha', \beta') \simeq (0.51, 0.05)$ for a (close to) toroidal polarization. These contours of Alfvén frequency match up excellently with the curves followed by the amplitude peak of the perpendicular velocity.

Figure 1h plots results from a separate simulation where the evolution of the second harmonic along the field line is considered. Plotted are color contours of $|B_\perp|$ in the equatorial plane, since for the second harmonic, the magnetic field perturbation has a maximum at the equator. To set this up the field-aligned dependence of the initial condition, given by Equations 2 and 3, is simply adjusted to $\sin(\pi\gamma/\gamma_{max})$. In this case, the curves traced turn from poloidal to toroidal over a shorter radial distance than for the fundamental. This is because the difference between the poloidal and toroidal frequencies is much less for the second harmonic. Again contours of constant Alfvén frequency match up favorably with the peaks in $|B_\perp|$.

To help with understanding these somewhat complicated patterns, Figure 2 describes the situation pictorially in the equatorial plane. Consider a start location in α (labeled L shell) where the initial polarization is poloidal. This is the dashed line labeled as the poloidal surface in the figure (recall that the medium is invariant in azimuth). For the dipole field used here, at any one location, the toroidal frequency is greater than the poloidal. Hence, moving outward in L shell to where the field lines are longer, in order to oscillate at the same frequency, a change of polarization from poloidal to toroidal will be required. The black lines are contours of Alfvén frequency for a fundamental field-aligned mode. For this given frequency, the sketched poloidal and toroidal surfaces (dashed lines) enclose the Resonant Zone (Wright & Elsden, 2016), outside of which no solutions exist. To restate this, the Alfvén frequency is constant along the black lines, when the Alfvén wave's polarization is such that the wave's velocity and magnetic field perturbations are tangential to the curves in Figure 2. For the second field-aligned harmonic, contours are sketched in red. The Resonant Zone has a smaller radial width in this case since the difference between poloidal and toroidal Alfvén frequency is greatly reduced for higher harmonics. Therefore the red contour turns over to a toroidal polarization much more quickly, as seen in the simulations (Figure 1h). This implies that the effects of the curved geometry are more important for the fundamental. Despite the fact that the second harmonic is most often observed, there have been recent observations of the fundamental (Dai et al., 2013; Takahashi et al., 2013), to which these new results could be most effectively applied. This sketch (Figure 2) will be returned to when considering multiple wavelengths in azimuth.

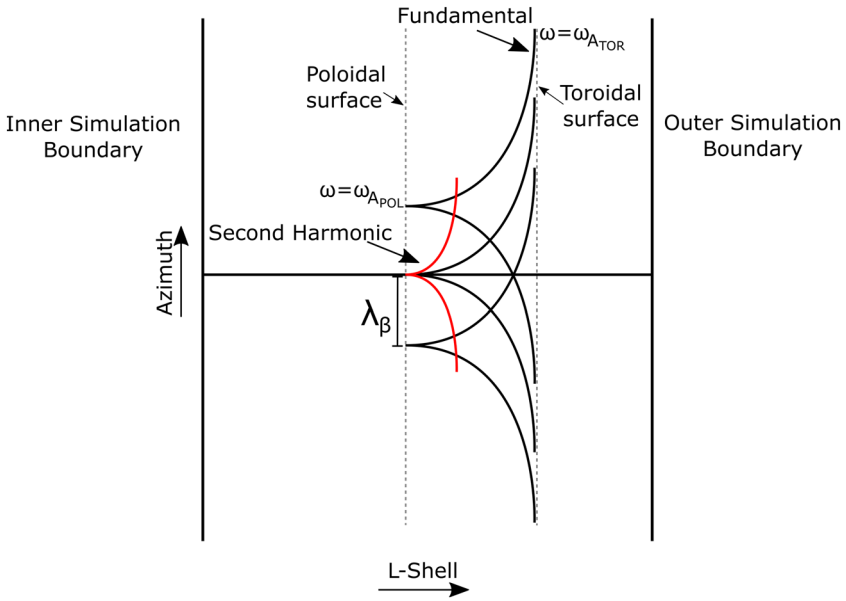

Figure 2. Sketch of the trajectories followed in the simulation, showing the contours of constant Alfvén frequency for the fundamental (black) and second harmonic (red) field-aligned modes. The dotted gray lines enclose the Resonant Zone for the fundamental.

3.1.3. Understanding the Polarization Change Mechanism

We have presented so far how the initially poloidal Alfvén wave undergoes a polarization rotation and have shown that it follows contours of Alfvén frequency in doing so, but what drives this process? We begin by looking at the field-aligned magnetic field component, B_γ, which describes magnetic field compression and represents the linear magnetic pressure. From previous Cartesian theory, we know that it is a small field-aligned magnetic field component generated through phase mixing, which couples the equations for the transverse velocities and permits the polarization rotation (Mann & Wright, 1995). Albeit small, it is the size of the perpendicular gradient of B_γ that will be important, which is of a higher order.

Figure 3 plots B_γ as a function of time at three locations along $\beta=0$: (a) $(\alpha,\ \beta)=(0.4, 0.0)$, (b) $(\alpha,\beta)=(0.45, 0.0)$, and (c) $(\alpha,\beta)=(0.5, 0.0)$. Each signal is reasonably monochromatic and decays as the wave packet moves away from the region around $\beta=0$ as displayed by the evolution shown in Figure 1. Figure 3d shows fast Fourier transforms (FFTs) of these time series. The vertical straight lines indicate the local poloidal Alfvén frequency at each location, which decreases with increasing radial distance (longer field lines), calculated by solving Equation 7. It is clear that the response of the compressional magnetic field in each case is generated at the local poloidal Alfvén frequency.

To better understand this, we consider the Alfvén wave polarization properties and the corresponding gradients in the magnetic pressure, which are responsible for driving Alfvén waves (e.g., Wright, 1994). Figure 4a displays a zoomed-in version of Figure 1e. Overlaid are velocity vectors as black arrows, which show that the velocity is polarized along the constant Alfvén frequency curves. This was first shown to occur by Wright and Elsden (2016) (their Figure 4). Hence we can picture the motion of plasma back and forth along these curves throughout an Alfvén wave period. Figure 4b displays as a color contour the compressional magnetic field component B_γ in the equatorial plane, with arrows corresponding to the vector $\Delta_\perp B_\gamma=(\partial B_\gamma/\partial\alpha, \partial B_\gamma/\partial\beta)$, to highlight the structure of the magnetic pressure gradient. For strong resonant excitation, we would require a magnetic pressure gradient aligned with the resonant surface. This can be pictured in a 1-D Cartesian sense as requiring a fast mode with a nonzero k_y to drive a toroidal field line resonance (large-amplitude U_y). However, in Figure 4b, the stronger gradients are present across the resonant surfaces rather than along them, suggesting that $U_{\alpha'}$ should be the largest velocity. This surprising feature can be resolved by considering the large k_y poloidal Alfvén wave result of Mann and Wright (1995).

They showed that the fields satisfy the ordering $u_x\sim b_x\sim O(1)$, $u_y\sim b_y\sim O(1/k_y)$, and $b_z\sim O(1/k_y^2)$. Wright and Elsden (2016) explain how this would translate to $U_{\beta'}\sim B_{\beta'}\gg U_{\alpha'}\sim B_{\alpha'}\gg B_\gamma$ in Figure 4. Hence B_γ is so small that the gradient in the α' direction only drives a small $U_{\alpha'}$ despite the small scale in α'. This begs

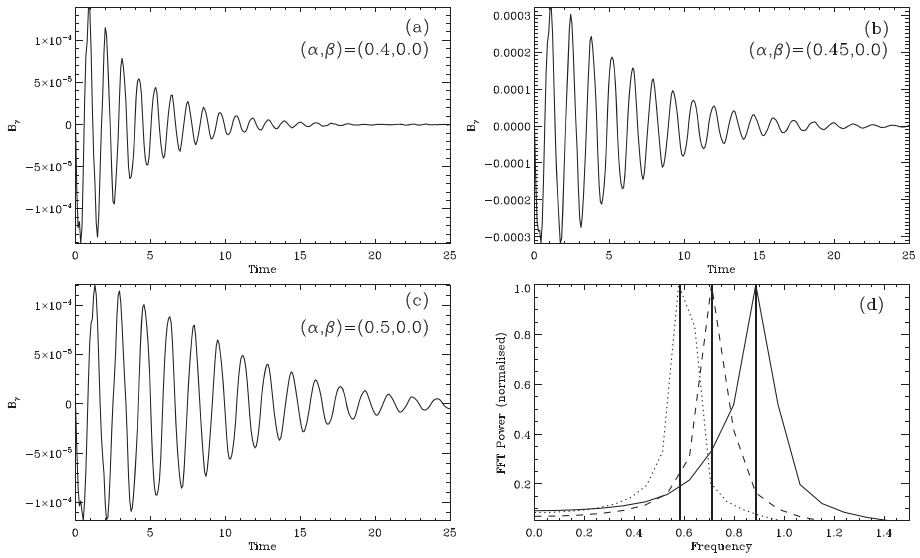

Figure 3. (a–c) Time series of B_γ at different locations in α (0.4, 0.45, and 0.5) at $\beta = 0$. (d) FFTs of each of the time series (dotted—panel c; dashed—panel b; and solid—panel a), with vertical lines at the local poloidal Alfvén frequency.

the question why $U_{\beta'} \gg U_{\alpha'}$ given the pressure gradient along β' is much less than in α'? The reason is that the β' direction is unique in that ω_A for a wave polarized along β' matches the frequency of the magnetic pressure—hence it is driven resonantly.

To interpret the relationship between the driver (magnetic pressure gradient along Alfvén frequency contour, $\partial B_\gamma/\partial\beta'$) and the response (transverse velocity aligned with Alfvén frequency contour, $U_{\beta'}$), we consider how these quantities are related at three different points along the same contour, shown in Figure 5. The left column plots the variation of $U_{\beta'}$ (black) and $-\partial B_\gamma/\partial\beta'$ (red) with time. The negative sign is included since this is the overall force that drives the system. The top left panel (Figure 5a) is taken from the location $(\alpha, \beta) = (0.45, 0.0)$ at the center of the peak of the initial condition. The polarization here taken from the direction of the Alfvén frequency contour is $\theta = 1.519$, measured from the β axis such that $\theta = 0$ implies a toroidal polarization, $\theta = \pi/2$ poloidal. From this location, the velocity is seen to decrease in time as the wave packet travels away from the central region. The magnetic pressure gradient in red at first increases, generated by the compression from phase mixing, but then decreases. The phase relation between these components is striking, clearly remaining out of phase for all time. This is depicted in the corresponding

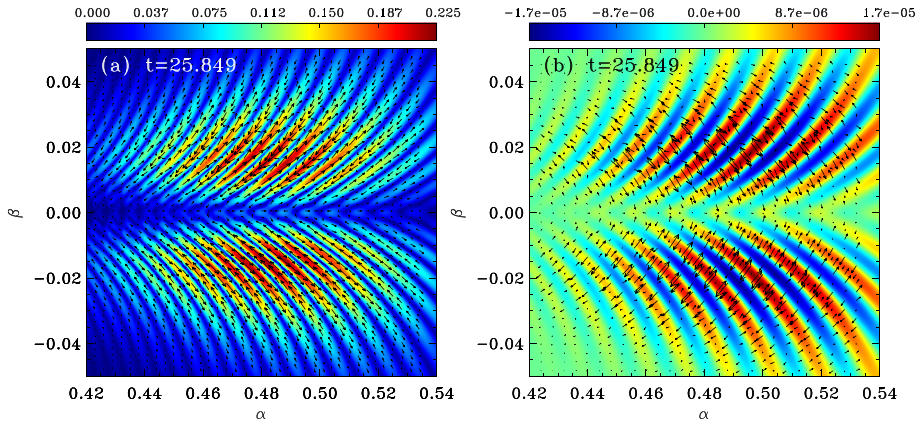

Figure 4. (a) Contour plot of $U_\perp$ in the equatorial plane with overlaid velocity vectors showing the wave polarization. (b) Contour of B_γ, the compressional magnetic field perturbation, in the equatorial plane with vectors $\Delta_\perp B_\gamma$, showing the strength and direction of the magnetic pressure gradient.

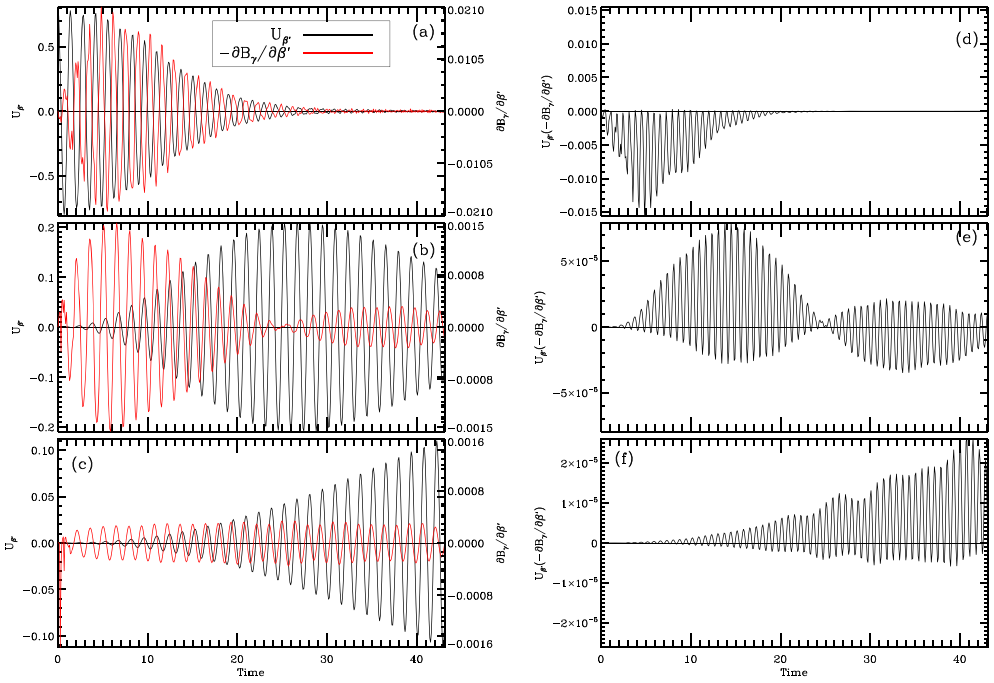

Figure 5. Time series of velocity (U'_β—black) and the negative magnetic pressure gradient ($-\partial b_\gamma/\partial\beta'$—red) aligned with a contour of Alfvén frequency at three locations along the same particular contour: (a) $(\alpha, \beta) = (0.45, 0.0)$, $\theta = 1.519$; (b) $(\alpha, \beta) = (0.487, 0.019)$, $\theta = 0.820$; and (c) $(\alpha, \beta) = (0.51, 0.052)$, $\theta = 0.391$. (d–f) Product of the time series in the panels on the left to demonstrate the rate at which work is done on the plasma.

top panel of the right column (Figure 5d), where the product of these two quantities is plotted. This represents the work done ($\mathbf{F} \cdot \mathbf{v}$) on the system. Clearly there is energy being taken out of the Alfvén wave at this location, which fits with the picture of the wave packet leaving this location in time.

The middle left panel (Figure 5b) is taken from $(\alpha, \beta) = (0.487, 0.019)$, which is an intermediate point along the contour emanating from the first location. At this point, $\theta = 0.820$ implying a mixed polarization. Here the amplitude first increases, then reaches a maximum ($t \approx 25$), and then starts to decrease. This is consistent with the peak of the wave packet approaching and then passing over this location. It is also consistent with the time average (over one cycle) of $\mathbf{F} \cdot \mathbf{v}$ being positive ($t < 25$) and then negative ($t > 25$) indicating there is a net input of energy to the Alfvén wave followed by removal (Figure 5e).

The bottom left panel (Figure 5c) is taken from $(\alpha, \beta) = (0.51, 0.052)$, $\theta = 0.391$, still on the same contour, toward where the amplitude peak of the wave packet has reached by the end of the simulation. Here there is a consistent steady driving of the velocity, with a near constant amplitude and phase relation between the driver and the response, resulting in the resonant growth of the velocity perturbation. This is corroborated by the predominantly positive product in Figure 5f and fits with the amplitude peak gradually moving toward this location. Comparing these terms at the three different locations clearly shows a causal relationship and points to the generation of compression as the driver of the movement along the contour.

3.1.4. Lifetimes of Poloidal Alfvén Waves

A prediction from previous theory for the Cartesian box model case is that the initial poloidal mode will have a finite lifetime (Mann & Wright, 1995), before it rotates to a toroidal polarization. Furthermore, this lifetime will scale linearly with the azimuthal wavenumber: The larger the azimuthal wavenumber (i.e., the more dominant the initial poloidal polarization), the longer the mode remains dominantly poloidal. Given the different magnetic geometry in our case, we wanted to compare with this theory, to see if the underlying mechanism is essentially still the same. To do so, five simulations were run with different azimuthal wavenumbers, ranging from $m \sim 40$ to $m \sim 300$. The dimensionless simulation wavenumbers used were converted into realistic m values for the magnetosphere, by assuming a normalizing length scale of $L_0 = 10\ R_E$. It is then used that $m = k_\beta R$, for angular azimuthal wavenumber k_β and radial distance R. For example, a dimensionless azimuthal wavelength of 0.02, as used in Figure 1, corresponds to a real length

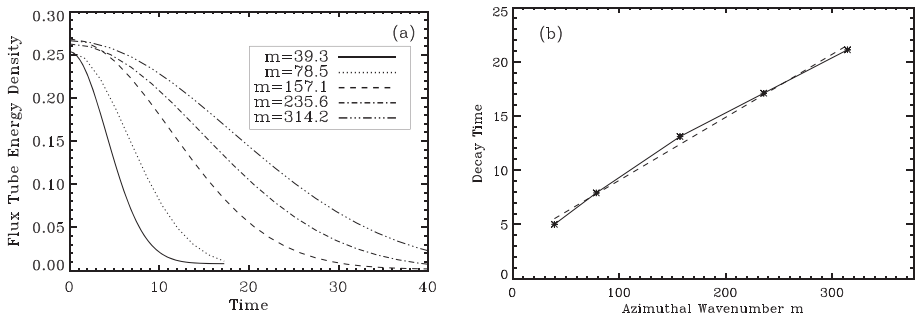

Figure 6. (a) Square root of the flux tube energy density (FTED) at $(\alpha, \beta) = (0.45, 0.0)$, from five simulations with different m numbers as listed in the plot legend. For context, a time of 10 time units corresponds to ~7.5 poloidal wave periods. (b) Star symbols represent the time for the FTED to decay by half in each of the different runs. Dashed line represents a linear fit to the data.

of 0.2 R_E, such that $k_\beta = 2\pi/\lambda_\beta = 31.416$. Therefore, at $L = 5$, the azimuthal wavenumber m is given by $m = 31.416 \times 5 = 157.08$.

Measuring the timescale for the transition from poloidal to toroidal is much more difficult here than in the straight field case, since you can no longer simply sit at one location and check the time at which the poloidal and toroidal energies are the same (see Figure 4 of Mann & Wright, 1995). Further, the rotation now depends upon the structure of the contours of Alfvén frequency, as shown in Figure 1. Hence, we instead choose to measure the time it takes for the energy in the initial poloidal mode to decay by half, due to the amplitude peak of the wave packet having moved away along the Alfvén frequency contours. We form the flux tube energy density (FTED) (Elsden & Wright, 2017), which represents the total energy integrated in γ along a flux tube of unit cross section in the equatorial plane, and take the square root of this quantity. This can be written at a particular time as

$$FTED(\alpha, \beta) = \int_{\gamma=0}^{\gamma=\gamma_{max}} \left\{ \frac{h_\alpha h_\beta h_\gamma}{h_\alpha(\gamma=0) h_\beta(\gamma=0)} \left(\frac{\rho}{2}(u_\alpha^2 + u_\beta^2) + \frac{1}{2}(b_\alpha^2 + b_\beta^2 + b_\gamma^2) \right) \right\} d\gamma, \tag{9}$$

for scale factors h_α, h_β, and h_γ and density ρ, which is inferred from the chosen Alfvén speed and background magnetic field. Figure 6a shows the square root of the FTED against time taken from the peak of the initial condition $((\alpha, \beta) = (0.45, 0.0))$, in five simulations with different m numbers as listed in the plot legend. The half-width time of these profiles is then plotted in Figure 6b as a function of azimuthal wavenumber. This shows that the relation is approximately linear for large m, but does not pass through the origin, so is different from the Cartesian case.

3.1.5. Rate of Motion Along Alfvén Frequency Contours

Another facet of this problem is to determine the rate at which the initially poloidal wave travels along contours of Alfvén frequency. Previous theory suggests that the "time taken by the wave to approach the toroidal surface is infinite" (Leonovich & Mazur, 1993). To measure this we can track the motion of the maximum amplitude of the wave packet along the contour, measured by the FTED peak. Figure 7a plots the distance traveled along the contour by this peak in time as the solid line. The dashed line is simply a linear fit to the initial motion. It is clear that the motion is indeed slowing down, in accord with the theory of Leonovich and Mazur (1993). Due to numerical restrictions caused by a continually decreasing phase-mixing length, we were unable to see if the wave ever would reach the toroidal surface. However, based on the assumption that it is the small amount of compression driving the procession along the Alfvén frequency contour, we would argue that once the ratio of perpendicular scale sizes becomes such that next to no compression is generated, the wave may remain at one location. This discussion is essentially academic, given that the wave would be comfortably dissipated, or smaller-scale processes would have become important enough, by the time of potentially reaching the toroidal surface. Figure 7b is produced for simulations using multiple wavelengths in azimuth and will be referred back to in later sections.

3.2. Multiple Azimuthal Wavelengths (Standing)

The simulation presented in the previous section of a single azimuthal wavelength has been critical for understanding the physics of the problem. However, in reality, poloidal Alfvén waves do not exist in the magnetosphere as single isolated structures but can instead cover a large longitudinal extent, for example,

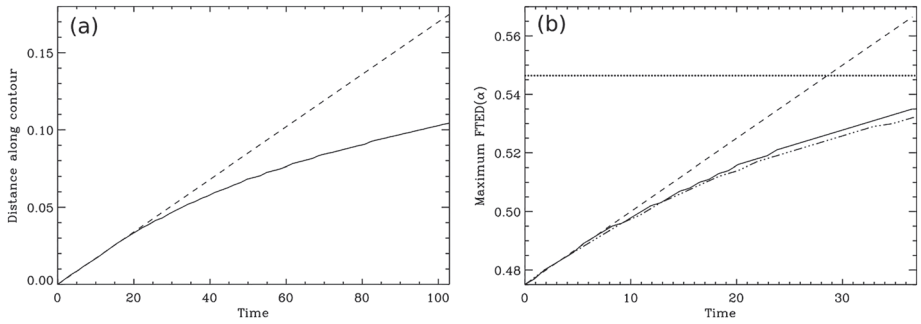

Figure 7. (a) Tracking the amplitude peak of the flux tube energy density (FTED) in time, indicating the distance traveled along a resonant contour. The dashed line is a fit to the early time behavior. (b) Location of maximum FTED in α in the azimuthally standing multiwavelength (dot-dashed) and the azimuthally propagating (solid) simulations. Dashed line is a linear fit to early time motion, and horizontal dotted line is the α location of the toroidal resonant surface for $\omega_{A_{tor}}(\alpha) = \omega_{A_{pol}}(\alpha = 0.475)$, to which the curved lines should asymptote.

over 1.5 to 8 hr in MLT (Engebretson et al., 1992). To this end, we adjusted the initial condition to consider a wave packet, still standing in azimuth, but containing 10 wavelengths. Figure 8a displays the initial condition for U_α, the radial velocity in the equatorial plane. This is achieved by simply using an azimuthal dependence of $\cos(k_\beta \beta)$ for the central portion, which then tapers smoothly off at each end of the wave packet.

Figure 8b displays the magnitude of $|U_\perp|$ in the equatorial plane, at a later time in the simulation ($t = 18.3$). Phase mixing has, as in the single wavelength case, generated smaller scales and forced a polarization rotation. At each location in azimuth, the waves are following contours of Alfvén frequency, which then overlap with contours emanating from neighboring start locations. It is like superposing several simulations as shown in Figures 1a and 1c–1f with each shifted in azimuth to produce the initial state in Figure 8a. This overlapping generates an interference pattern as seen in Figure 8b. This can be explained by the sketch in Figure 2, where contours (black curves) emanating from the poloidal surface from different locations in β cross at some point in the Resonant Zone. The azimuthal wavelength λ_β, together with the structure of the Alfvén frequency contours, will determine where such a crossing occurs.

We can consider how a satellite would perceive the intricate patterns shown in Figure 8b, by looking at velocity hodograms to determine the polarization at different times throughout the Alfvén wave evolution. Figure 9 displays velocity hodograms from three different simulations: panels (a) and (b) from the single wavelength simulation discussed in the previous section (Figures 1a and 1c–1f); panels (c) and (d) from the multiple wavelength azimuthally standing simulation (this section); and panels (e)–(h) from multiple

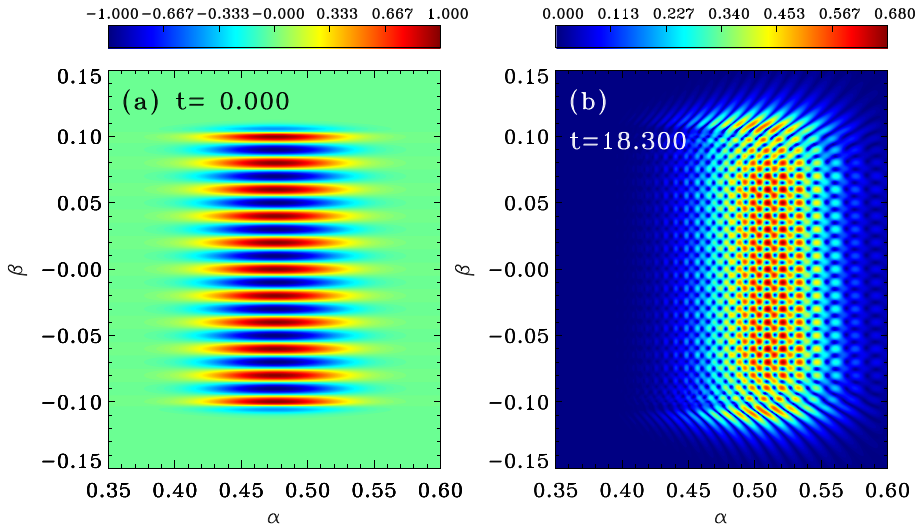

Figure 8. (a) Contours of the initial condition U_α in the equatorial plane, using multiple wavelengths in azimuth. (b) Resulting perpendicular velocity $|U_\perp|$ distribution at $t = 18.3$.

wavelength azimuthally propagating simulation to be discussed in the following section. In each plot the red trace is from an early time, green an intermediate time, and blue at a later time. Focus first on Figure 9a, taken from the center of the initial condition at $(\alpha, \beta) = (0.45, 0.0)$, in the single wavelength simulation. The red curve (time $t = 0 \rightarrow 1.38$) shows the dominant poloidal polarization of the initial condition. Over time, the wave decays while maintaining a poloidal polarization, as evidenced by the decreasing amplitude of the green ($t = 8.62 \rightarrow 10.08$) and blue ($t = 17.23 \rightarrow 18.70$) traces. This is consistent with the decay present in the black curve time series from Figure 5a. Figure 9b is taken from a point outside of the region of the initial condition, at $(\alpha, \beta) = (0.465, 0.01)$. Here the wave begins nearly poloidally polarized but of small amplitude (red curve). As time progresses and the wave packet moves along the Alfvén frequency contours, the amplitude increases at this location, accompanied by a significant change in the polarization (blue).

Figure 9c, from the multiple wavelength azimuthally standing case, shows the hodogram signatures at the center of the initial condition region, which in this simulation is $(\alpha, \beta = 0.475, 0.0)$. The wave is initially strongly poloidal (red) and remains so for most of its evolution (green and blue curves). This is somewhat surprising, given the apparent interference along contours of Alfvén frequency shown in Figure 8b. Clearly, however, the fact that the mode is standing in the β direction, and this location is a node of U_β, means it remains dominantly poloidal. Figure 9d is taken from a slightly different azimuthal location $(\alpha, \beta = 0.475, 0.003)$, which causes a huge change to the hodogram signatures. The mode undergoes a much greater rotation over the same time periods (t: $1.83 \rightarrow 3.48$, t: $9.15 \rightarrow 10.80$, and t: $18.30 \rightarrow 19.95$). The hodograms in the right-hand column will be addressed in the next section.

3.3. Azimuthal Phase Motion (Propagating)

The final simulation of our study considers multiple wavelengths in azimuth, together with an azimuthal phase motion. This is added to reflect that high-m poloidal Alfvén waves are often excited by the drift or drift-bounce resonance mechanism (Southwood & Kivelson, 1981, 1982; Southwood et al., 1969), as discussed at length in section 1. This mechanism has been used to explain a plethora of observations of high-m poloidal ULF waves with azimuthal phase propagation (e.g., Dai et al., 2013; Ozeke & Mann, 2008; Shi et al., 2018; Takahashi et al., 1990).

To construct the initial condition, we write a propagating wave as the sum of two standing wave solutions, for example,

$$\cos(k_\beta \beta + \omega t) = \cos(k_\beta \beta)\cos(\omega t) - \sin(k_\beta \beta)\sin(\omega t). \tag{10}$$

The previous azimuthally standing initial conditions, as described in Equations 2 and 3, represented a temporal dependence of $\cos(\omega t)$ for the velocity components (i.e., maximum value at $t = 0$). This satisfies $B_\perp(t = 0) = 0$, given that $B_\perp \sim \partial U_\perp / \partial t \sim \sin(\omega t)$. However, adding the $\sin(\omega t)$ term into the initial condition for $U_\perp$ (as shown in Equation 10) for a propagating solution will require the setting of a nonzero $B_\perp$ term. The easiest way to do this consistently was to let the simulation give the answer in the following way. We used the same initial condition as for the multiwavelength standing case, defining only the perpendicular velocity. This simulation was then run for a time of a quarter period at the poloidal Alfvén frequency of the central point of the initial condition ($\alpha = 0.475$, $\beta = 0.0$). The $B_\perp$ components were stored from this snapshot and used at $t = 0$ to start the real simulation. This gives $B_\perp$ components consistent with the $\sin(\omega t)$ part of the initial condition for the velocity components. Further required is a "slipping" of the $B_\perp$ solution in the β direction, by a quarter of a wavelength. This accounts for the different β dependence between the second and third terms of Equation 10 and provides the required azimuthal phase motion.

The results of using such an initial condition are shown in Figure 10, displaying color contour plots of $|U_\perp|$ in the equatorial plane. Figure 10a at $t = 0.0$ displays the initial condition. Subsequent panels show how this wave packet evolves in time, when there is a phase motion in the negative β direction. The wavefronts have inclined significantly by time $t = 6.863$ in Figure 10b, and this inclination continues throughout the evolution in Figures 10c and 10d, creating a very different picture to the azimuthally standing case in Figure 8b. For reference, the poloidal wave period at $\alpha = 0.475$ is $\tau_{pol} = 1.484$.

To explain the inclination of these phase fronts, we consider how phase mixing governs the wave evolution. The fields phase mix according to $\exp(i\Phi)$, where

$$\Phi = \omega_A(\alpha, \theta)t + k_\beta \beta, \tag{11}$$

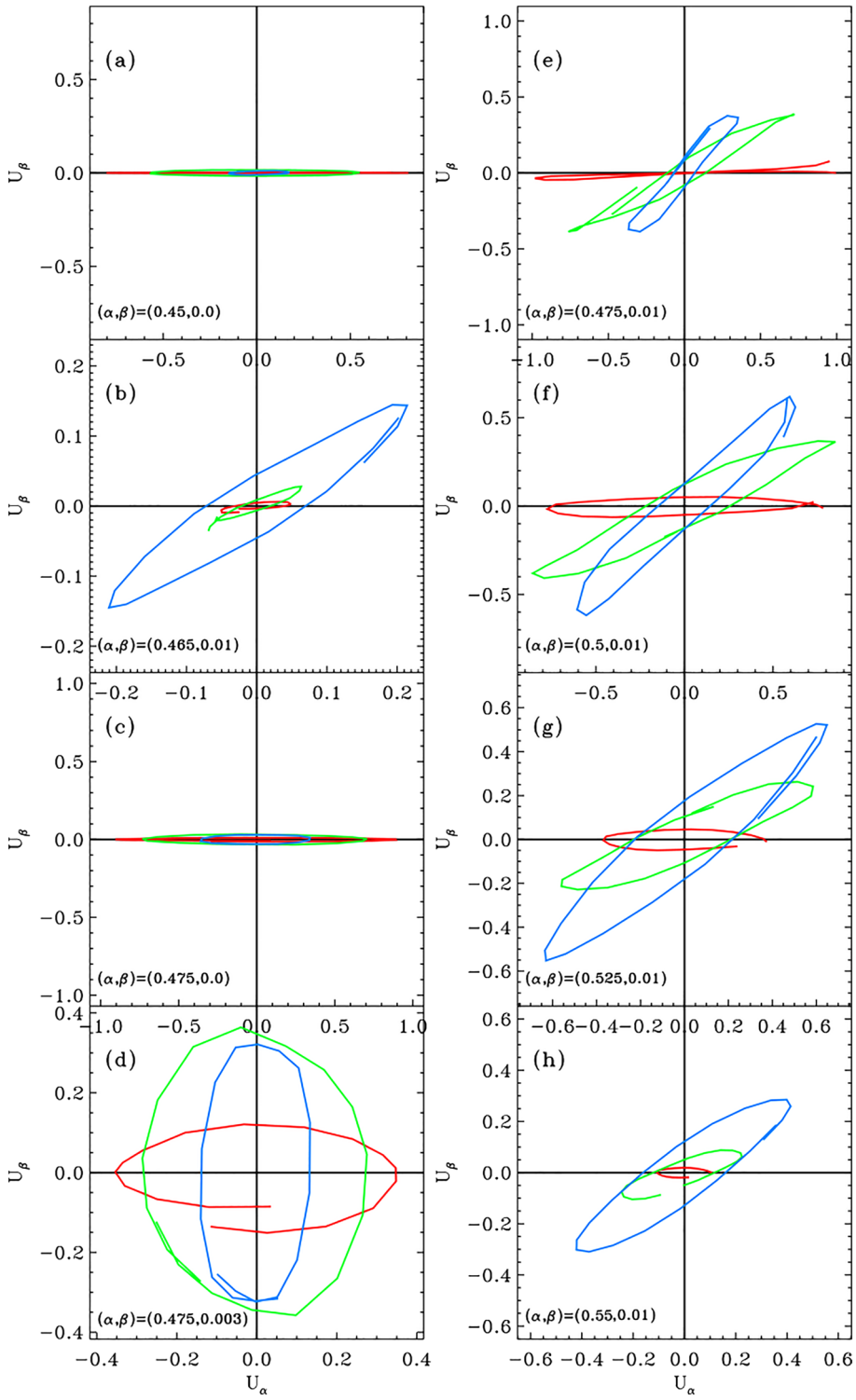

Figure 9. Hodograms of the perpendicular velocity in the equatorial plane from three simulations presented in this paper. Single wavelength in azimuth—panels (a) and (b); multiwavelength azimuthally standing—panels (c) and (d); and multiwavelength azimuthally propagating—panels (e)–(h). The (α, β) locations are given in the bottom left corner of each panel. Different periods are traced by the different colors: red earliest, green intermediate, and blue latest.

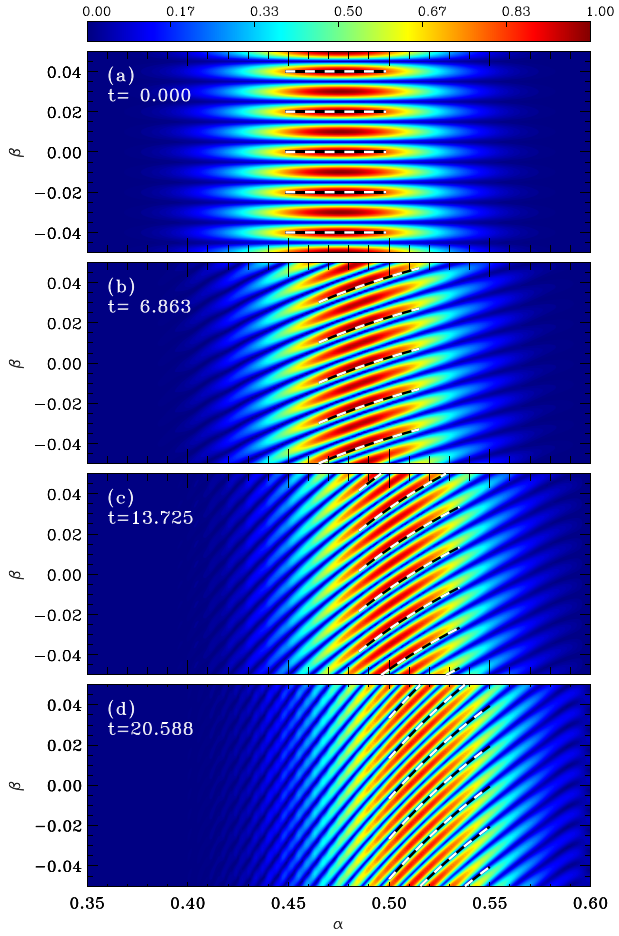

Figure 10. Contours of $|U_\perp|$ in the equatorial plane for the simulation with azimuthal phase propagation at different times as listed on each panel. Overplotted dashed lines represent a fit to the slope of the lines, described in the main text.

with $\theta = \theta(\alpha, t)$, such that $\Phi = \Phi(\alpha, \beta, \theta, t)$. For a given snapshot ($dt = 0$), a small change in Φ can be written as

$$d\Phi = \left(\frac{\partial \omega_A}{\partial \alpha}\bigg|_\theta d\alpha + \frac{\partial \omega_A}{\partial \theta}\bigg|_\alpha \frac{\partial \theta}{\partial \alpha}\bigg|_t d\alpha \right) t + k_\beta d\beta. \tag{12}$$

The ridges in Figure 10 have the property that Φ is constant, so setting $d\Phi = 0$ implies

$$\frac{d\beta}{d\alpha} = -\left(\frac{\partial \omega_A}{\partial \alpha}\bigg|_\theta + \frac{\partial \omega_A}{\partial \theta}\bigg|_\alpha \frac{\partial \theta}{\partial \alpha}\bigg|_t \right) \frac{t}{k_\beta}. \tag{13}$$

The wave polarization angle θ aligns with the ridges according to

$$\theta = \tan^{-1}\left(\frac{d\alpha}{d\beta} \right). \tag{14}$$

Equations 13 and 14 show how the location in β can be determined as a function of α and time, which is all the information required to track the phase fronts.

Begin with the poloidal solution at $t = 0$, whereby $d\beta/d\alpha = 0$, such that Equation 14 gives $\theta(\alpha, t = 0) = \pi/2$. This can be used in the rhs of (13) to move from say location (α_0, β_0) to $(\alpha_0 + d\alpha, \beta_0 + d\beta)$ and repeated to form one of the dashed lines in Figure 10. Initially this gives the horizontal lines in Figure 10a.

Advancing in time, Equation 13 will give nonzero $d\beta/d\alpha$ and (14) the corresponding θ. In this way we have a procedural method to determine the dashed lines for all subsequent times t_{n+1} using the estimate of the

polarization angle at the previous time t_n. Such lines, as overlaid in Figure 10, clearly give a good match to the observed phase fronts.

As for the previous simulations, we consider the hodogram signatures at different locations in the domain, shown in the right-hand column of Figures 9e–9h. Moving from top (Figure 9e) to bottom (Figure 9h) represents moving outward radially. Each panel shows a similar trend, with the initial poloidal polarization (red) rotating to an intermediate polarization (blue) by a later time. This is expected from the orientation of the phase fronts in Figure 10. The radially outward motion of the wave packet is also evident, with the top panel showing a decrease in the wave amplitude over time, while the bottom panels show an increase.

This radially outward motion can also be seen in Figure 7b, where the α location of the maximum FTED is plotted against time, for both the multiple wavelength azimuthally standing (dot-dashed) and propagating (solid) simulations. The dashed line is a linear fit to the early time motion and shows, as in the single azimuthal wavelength case, that the motion along Alfvén frequency contours is slowing down. The horizontal dotted line represents the location in α where the toroidal mode has the same frequency as the poloidal mode at the center of the initial condition, that is, where $\omega_{A_{tor}}(\alpha) = \omega_{A_{pol}}(\alpha = 0.475)$. This occurs at $\alpha = 0.5465$, and it can be seen that the curves are tending toward this line, as expected for the given polarization rotation.

Besides the obvious drift of the waves in Figure 10 to larger α, there is also a gradual drift of the waves to larger β. (This is not evident in Figure 10 as we focus on the central section in β of the wave packet.) Alfvén waves are commonly thought to be strictly confined to a particular field line, so it is perhaps surprising that they can drift to neighboring field lines.

The resolution lies in the observation of Singer et al. (1981) that Alfvén waves are strictly decoupled (and so remain on their original field line) if $B_\gamma = 0$—that is, there is no magnetic pressure perturbation. This is the case for an axisymmetric $m = 0$ toroidal Alfvén wave. However, for the waves considered here, $B_\gamma \neq 0$, albeit small. Such Alfvén waves have been described as asymptotically decoupled (Mann et al., 1997; Wright, 1992; Wright & Elsden, 2016) in the sense that there is (almost) no magnetic pressure, so they appear to be decoupled Alfvén waves at early times. Over a longer timescale, the fact that they are not truly decoupled becomes evident as the presence of a small magnetic pressure allows neighboring field lines to communicate and is associated with a nonzero perpendicular component of the Poynting vector.

4. Conclusions

We have studied the evolution of high-m poloidal ULF waves in a dipole magnetic field numerically, in the framework of cold, linear MHD. A list of our conclusions is given below together with areas open to future research.

1. In a dipole magnetic field, where the poloidal and toroidal Alfvén eigenfrequencies differ substantially, an initially poloidal high-m Alfvén wave will not simply rotate to a toroidal polarization as per the Cartesian straight field theory. Instead the Alfvén wave will drift along contours along which the polarization varies from poloidal toward toroidal, and the Alfvén frequency for these locations and polarizations is constant. This will cause a radially outward motion of the wave packet, something that could be considered in satellite data.
2. This effect will be most visible for the fundamental mode along the field line, and depending upon the equilibrium could be important for the second harmonic too.
3. We posit that phase mixing generates a small amount of compression, which couples the transverse components of the velocity and drives the polarization rotation. This occurs at the frequency of the initial poloidal mode, meaning that waves are forced to follow contours of Alfvén frequency with varying polarization to continue to match this seed frequency.
4. The length of time taken to perform the rotation scales approximately linearly with the azimuthal wavenumber, with larger-m modes taking longer to rotate. This reinforces phase mixing as the underlying driving mechanism.
5. When azimuthal phase motion is considered, this combines with the motion along Alfvén frequency contours to create differently shaped phase fronts. We have provided approximate formulae for such fronts.

6. Hodograms for this case display a polarization rotation at all locations in the domain, together with the overall radially outward motion of the amplitude peak. These are spatial and temporal features that could be investigated in satellite data.

Some final notes on the limitations of this study and potential future avenues of research. We have not considered how this system is driven, merely the resulting evolution of an undriven poloidal Alfvén wave. Future numerical studies could consider the driving of this system, for example, by a consistent non-Maxwellian particle distribution (e.g., Baddeley et al., 2005), or by a moving cloud of energetic particles (Mager & Klimushkin, 2008), to better match observations. Certainly, inclusion of such drivers would complicate the polarization evolution (Wei et al., 2019).

On observations, we have made no attempt here to match to particular elements of any one observation but have placed the work in the context of current observational understanding of high-m ULF waves. The point of this work is to better understand the underlying physics, leaving observational comparison to a future study. In such a study, retrieving accurate polarization information will be key for identifying the predicted rotation, for example, through a conjunction of spacecraft and radar data (e.g., Shi et al., 2018). However, we have made some predictions as to how consideration of the curved magnetic geometry will affect the observed wavefields.

Another aspect not considered here is full 3-D inhomogeneity, in both the magnetic field and plasma density. This will greatly affect the dynamics of this process given the substantial change to contours of Alfvén frequency that such complexity will bring. For example, adding a radially varying Alfvén speed profile will considerably affect the rates of phase mixing, as well as expanding or contracting the Resonant Zone. A particular case, which has been identified previously in observations where this will be important, is when there are localized dips in the poloidal Alfvén frequency with L shell (Denton et al., 2003). Such dips have been used to explain observations of a consistent poloidal frequency across a substantial range in L shell (Takahashi et al., 1987). In regions where the frequency is not sharply varying, the Resonant Zone will be significantly expanded, causing the Alfvén frequency contours to have a much larger radial extent. This will mean that the polarization rotation discussed in this study will contribute to a far more significant radially outward motion.

Data Availability Statement

Data used to produce the simulation plots can be accessed online (https://figshare.com/authors/Tom_Elsden/4743264).

Acknowledgments
T. Elsden was funded by an Early Career Fellowship, split jointly by the Leverhulme Trust (ECF-2019-155) and the University of Leicester. A. Wright was partially funded by the Science and Technology Facilities Council (STFC) grant (ST/N000609/1). The research in this paper was completed as part of the activities of an International Team sponsored by the International Space Science Institute (ISSI, Bern). The authors are grateful to ISSI for supporting this work.

References

Anderson, B. J., Engebretson, M. J., Rounds, S. P., Zanetti, L. J., & Potemra, T. A. (1990). A statistical study of Pc 3–5 pulsations observed by the AMMPTE/CCE Magnetic Fields Experiment, 1. Occurrence distributions. *Journal of Geophysical Research*, *95*(A7), 10,495–10,523. https://doi.org/10.1029/JA095iA07p10495

Baddeley, L. J., Yeoman, T. K., & Wright, D. M. (2005). HF doppler sounder measurements of the ionospheric signatures of small scale ULF waves. *Annales Geophysicae*, *23*(5), 1807–1820. https://doi.org/10.5194/angeo-23-1807-2005

Dai, L., Takahashi, K., Lysak, R., Wang, C., Wygant, J. R., Kletzing, C., et al. (2015). Storm time occurrence and spatial distribution of Pc4 poloidal ULF waves in the inner magnetosphere: A Van Allen Probes statistical study. *Journal of Geophysical Research: Space Physics*, *120*, 4748–4762. https://doi.org/10.1002/2015JA021134

Dai, L., Takahashi, K., Wygant, J. R., Chen, L., Bonnell, J., Cattell, C. A., et al. (2013). Excitation of poloidal standing Alfvén waves through drift resonance wave-particle interaction. *Geophysical Research Letters*, *40*, 4127–4132. https://doi.org/10.1002/grl.50800

Denton, R. E., Lessard, M. R., & Kistler, L. M. (2003). Radial localization of magnetospheric guided poloidal Pc 4-5 waves. *Journal of Geophysical Research*, *108*(A3), 1105. https://doi.org/10.1029/2002JA009679

Elkington, S. R., Hudson, M. K., & Chan, A. A. (2003). Resonant acceleration and diffusion of outer zone electrons in an asymmetric geomagnetic field. *Journal of Geophysical Research*, *108*(A3), 1116. https://doi.org/10.1029/2001JA009202

Elsden, T., & Wright, A. N. (2017). The theoretical foundation of 3-D Alfvén resonances: Time-dependent solutions. *Journal of Geophysical Research: Space Physics*, *122*, 3247–3261. https://doi.org/10.1002/2016JA023811

Elsden, T., & Wright, A. N. (2018). The broadband excitation of 3-D Alfvén resonances in a MHD waveguide. *Journal of Geophysical Research: Space Physics*, *123*, 530–547. https://doi.org/10.1002/2017JA025018

Elsden, T., & Wright, A. N. (2019). The effect of fast normal mode structure and magnetopause forcing on FLRs in a 3-D waveguide. *Journal of Geophysical Research: Space Physics*, *124*, 178–196. https://doi.org/10.1029/2018JA026222

Engebretson, M. J., Murr, D. L., Erickson, K. N., Strangeway, R. J., Klumpar, D. M., Fuselier, S. A., et al. (1992). The spatial extent of radial magnetic pulsation events observed in the dayside near synchronous orbit. *Journal of Geophysical Research*, *97*(A9), 13,741–13,758. https://doi.org/10.1029/92JA00992

Heyvaerts, J., & Priest, E. R. (1983). Coronal heating by phase-mixed shear Alfven waves. *Astronomy and Astrophysics*, *117*, 220–234.

Hughes, W. J., & Southwood, D. J. (1976). The screening of micropulsation signals by the atmosphere and ionosphere. *Journal of Geophysical Research*, *81*(19), 3234. https://doi.org/10.1029/JA081i019p03234

Hughes, W. J., Southwood, D. J., Mauk, B., McPherron, R. L., & Barfield, J. N. (1978). Alfven waves generated by an inverted plasma energy distribution. *Nature*, *275*, 43–45. https://doi.org/10.1038/275043a0

Jacobs, J. A., Kato, Y., Matsushita, S., & Troitskaya, V. A. (1964). Classification of geomagnetic micropulsations. *Journal of Geophysical Research*, *69*, 180–181. https://doi.org/10.1029/JZ069i001p00180

James, M. K., Yeoman, T. K., Mager, P. N., & Klimushkin, D. Y. (2013). The spatio-temporal characteristics of ULF waves driven by substorm injected particles. *Journal of Geophysical Research: Space Physics*, *118*, 1737–1749. https://doi.org/10.1002/jgra.50131

James, M. K., Yeoman, T. K., Mager, P. N., & Klimushkin, D. Y. (2016). Multiradar observations of substorm-driven ULF waves. *Journal of Geophysical Research: Space Physics*, *121*, 5213–5232. https://doi.org/10.1002/2015JA022102

Klimushkin, D. Y. (2007). How energetic particles construct and destroy poloidal high-*m* Alfvén waves in the magnetosphere. *Planetary and Space Science*, *55*(6), 722–730. https://doi.org/10.1016/j.pss.2005.11.006

Klimushkin, D. Y., Leonovich, A. S., & Mazur, V. A. (1995). On the propagation of transversally small-scale standing Alfven waves in a three-dimensionally inhomogeneous magnetosphere. *Journal of Geophysical Research*, *100*(A6), 9527–9534. https://doi.org/10.1029/94JA03233

Kokubun, S., Erickson, K. N., Fritz, T. A., & McPherron, R. L. (1989). Local time asymmetry of Pc 4-5 pulsations and associated particle modulations at synchronous orbit. *Journal of Geophysical Research*, *94*(A6), 6607–6625. https://doi.org/10.1029/JA094iA06p06607

Le, G., Chi, P. J., Strangeway, R. J., Russell, C. T., Slavin, J. A., Takahashi, K., et al. (2017). Global observations of magnetospheric high-*m* poloidal waves during the 22 June 2015 magnetic storm. *Geophysical Research Letters*, *44*, 3456–3464. https://doi.org/10.1002/2017GL073048

Leonovich, A. S., Klimushkin, D. Y., & Mager, P. N. (2015). Experimental evidence for the existence of monochromatic transverse small-scale standing Alfvén waves with spatially dependent polarization. *Journal of Geophysical Research: Space Physics*, *120*, 5443–5454. https://doi.org/10.1002/2015JA021044

Leonovich, A. S., & Mazur, V. A. (1993). A theory of transverse small-scale standing Alfvén waves in an axially symmetric magnetosphere. *Planetary and Space Science*, *41*(9), 697–717. https://doi.org/10.1016/0032-0633(93)90055-7

Mager, P. N., & Klimushkin, D. Y. (2006). On impulse excitation of the global poloidal modes in the magnetosphere. *Annales Geophysicae*, *24*(10), 2429–2433. https://doi.org/10.5194/angeo-24-2429-2006

Mager, P. N., & Klimushkin, D. Y. (2008). Alfvén ship waves: High-*m* ULF pulsations in the magnetosphere generated by a moving plasma inhomogeneity. *Annales Geophysicae*, *26*(6), 1653–1663. https://doi.org/10.5194/angeo-26-1653-2008

Mann, I. R., & Wright, A. N. (1995). Finite lifetimes of ideal poloidal Alfvén waves. *Journal of Geophysical Research*, *100*, 23,677–23,686. https://doi.org/10.1029/95JA02689

Mann, I. R., Wright, A. N., & Cally, P. S. (1995). Coupling of magnetospheric cavity modes to field line resonances: A study of resonance widths. *Journal of Geophysical Research*, *100*, 19,441–19,456. https://doi.org/10.1029/95JA00820

Mann, I. R., Wright, A. N., & Hood, A. W. (1997). Multiple-timescales analysis of ideal poloidal Alfvén waves. *Journal of Geophysical Research*, *102*, 2381–2390. https://doi.org/10.1029/96JA03034

Milan, S. E., Sato, N., Ejiri, M., & Moen, J. (2001). Auroral forms and the field-aligned current structure associated with field line resonances. *Journal of Geophysical Research*, *106*(A11), 25,825–25,834. https://doi.org/10.1029/2001JA900077

Min, K., Takahashi, K., Ukhorskiy, A. Y., Manweiler, J. W., Spence, H. E., Singer, J., et al. (2017). Second harmonic poloidal waves observed by Van Allen Probes in the dusk-midnight sector. *Journal of Geophysical Research: Space Physics*, *122*, 3013–3039. https://doi.org/10.1002/2016JA023770

Murphy, K. R., Mann, I. R., & Ozeke, L. G. (2014). A ULF wave driver of ring current energization. *Geophysical Research Letters*, *41*, 6595–6602. https://doi.org/10.1002/2014GL061253

Ozeke, L. G., & Mann, I. R. (2008). Energization of radiation belt electrons by ring current ion driven ULF waves. *Journal of Geophysical Research*, *113*, A02201. https://doi.org/10.1029/2007JA012468

Radoski, H. R. (1967). A note on oscillating field lines. *Journal of Geophysical Research*, *72*, 418–419. https://doi.org/10.1029/JZ072i001p00418

Radoski, H. R. (1974). A theory of latitude dependent geomagnetic micropulsations: The asymptotic fields. *Journal of Geophysical Research*, *79*, 595–603. https://doi.org/10.1029/JA079i004p00595

Sarris, T. E., Wright, A. N., & Li, X. (2009). Observations and analysis of Alfvén wave phase mixing in the Earth's magnetosphere. *Journal of Geophysical Research*, *114*, A03218. https://doi.org/10.1029/2008JA013606

Shi, X., Baker, J. B. H., Ruohoniemi, J. M., Hartinger, M. D., Murphy, K. R., Rodriguez, J. V., et al. (2018). Long-lasting poloidal ULF waves observed by multiple satellites and high-latitude SuperDARN radars. *Journal of Geophysical Research: Space Physics*, *123*, 8422–8438. https://doi.org/10.1029/2018JA026003

Singer, H. J., Hughes, W. J., & Russell, C. T. (1982). Standing hydromagnetic waves observed by ISEE 1 and 2: Radical extent and harmonic. *Journal of Geophysical Research*, *87*(A5), 3519–3529. https://doi.org/10.1029/JA087iA05p03519

Singer, H. J., Southwood, D. J., Walker, R. J., & Kivelson, M. G. (1981). Alfven wave resonances in a realistic magnetospheric magnetic field geometry. *Journal of Geophysical Research*, *86*, 4589–4596. https://doi.org/10.1029/JA086iA06p04589

Southwood, D. J. (1974). Some features of field line resonances in the magnetosphere. *Planetary Space Science*, *22*, 483–491. https://doi.org/10.1016/0032-0633(74)90078-6

Southwood, D. J., Dungey, J. W., & Etherington, R. J. (1969). Bounce resonant interaction between pulsations and trapped particles. *Planetary and Space Science*, *17*(3), 349–361. https://doi.org/10.1016/0032-0633(69)90068-3

Southwood, D. J., & Kivelson, M. G. (1981). Charged particle behavior in low-frequency geomagnetic pulsations 1. Transverse waves. *Journal of Geophysical Research*, *86*(A7), 5643–5655. https://doi.org/10.1029/JA086iA07p05643

Southwood, D. J., & Kivelson, M. G. (1982). Charged particle behavior in low-frequency geomagnetic pulsations 2. Graphical approach. *Journal of Geophysical Research*, *87*(A3), 1707–1710. https://doi.org/10.1029/JA087iA03p01707

Takahashi, K., Claudepierre, S. G., Rankin, R., Mann, I. R., & Smith, C. W. (2018). Van Allen Probes observation of a fundamental poloidal standing Alfvén wave event related to giant pulsations. *Journal of Geophysical Research: Space Physics*, *123*, 4574–4593. https://doi.org/10.1029/2017JA025139

Takahashi, K., Fennell, J. F., Amata, E., & Higbie, P. R. (1987). Field-aligned structure of the storm time Pc 5 wave of November 14–15, 1979. *Journal of Geophysical Research*, *92*, 5857–5864. https://doi.org/10.1029/JA092iA06p05857

Takahashi, K., Hartinger, M. D., Angelopoulos, V., Glassmeier, K.-H., & Singer, H. J. (2013). Multispacecraft observations of fundamental poloidal waves without ground magnetic signatures. *Journal of Geophysical Research: Space Physics*, *118*, 4319–4334. https://doi.org/10.1002/jgra.50405

Takahashi, K., McEntire, R. W., Lui, A. T. Y., & Potemra, T. A. (1990). Ion flux oscillations associated with a radially polarized transverse Pc 5 magnetic pulsation. *Journal of Geophysical Research*, *95*(A4), 3717–3731. https://doi.org/10.1029/JA095iA04p03717

Takahashi, K., Oimatsu, S., Nosé, M., Min, K., Claudepierre, S. G., Chan, A., et al. (2018). Van Allen Probes observations of second harmonic poloidal standing Alfvén waves. *Journal of Geophysical Research: Space Physics*, *123*, 611–637. https://doi.org/10.1002/2017JA024869

Wei, C., Dai, L., Duan, S., Wang, C., & Wang, Y. (2019). Multiple satellites observation evidence: High-*m* poloidal ULF waves with time-varying polarization states. *Earth and Planetary Physics*, *3*(3), 190–203. https://doi.org/10.26464/epp2019021

Wright, A. N. (1992). Asymptotic and time-dependent solutions of magnetic pulsations in realistic magnetic field geometries. *Journal of Geophysical Research*, *97*, 6439–6450. https://doi.org/10.1029/91JA02666

Wright, A. N. (1994). Dispersion and wave coupling in inhomogeneous MHD waveguides. *Journal of Geophysical Research*, *99*, 159–167. https://doi.org/10.1029/93JA02206

Wright, A. N., & Elsden, T. (2016). The theoretical foundation of 3D Alfvén resonances: Normal modes. *Astrophysical Journal*, *833*, 230. https://doi.org/10.3847/1538-4357/833/2/230

Wright, A. N., & Elsden, T. (2020). Simulations of MHD wave propagation and coupling in a 3-D magnetosphere. *Journal of Geophysical Research: Space Physics*, *125*, e27589. https://doi.org/10.1029/2019JA027589

Wright, A. N., Elsden, T., & Takahashi, K. (2018). Modeling the dawn/dusk asymmetry of field line resonances. *Journal of Geophysical Research: Space Physics*, *123*, 6443–6456. https://doi.org/10.1029/2018JA025638

Yeoman, T. K., James, M., Mager, P. N., & Klimushkin, D. Y. (2012). SuperDARN observations of high-*m* ULF waves with curved phase fronts and their interpretation in terms of transverse resonator theory. *Journal of Geophysical Research*, *117*, A06231. https://doi.org/10.1029/2012JA017668

Yeoman, T. K., Wright, D. M., & Baddeley, L. J. (2006). Ionospheric signatures of ULF waves: Active radar techniques. *Magnetospheric ULF waves: Synthesis and new directions* (Vol. 169, pp. 273). Washington, DC: American Geophysical Union. https://doi.org/10.1029/169GM18

Zalesak, S. T. (1979). Fully multidimensional flux-corrected transport algorithms for fluids. *Journal of Computational Physics*, *31*, 335–362. https://doi.org/10.1016/0021-9991(79)90051-2